Hexagonal approximant of the dodecagonal oxide quasicrystal on Pt(111)

M. Maniraj [ORCID],[*] L. V. Tran [ORCID], O. Krahn, S. Schenk, W. Widdra, and S. Förster [ORCID][†]

Institute of Physics, Martin-Luther-Universität Halle-Wittenberg, D-06099 Halle, Germany

Quasicrystals (QC) in condensed matter are often accompanied by competing periodic structures with large unit cells that approximate the QC. Likewise for the dodecagonal Ba-Ti-O oxide quasicrystal that forms on Pt(111), approximants with square and oblique lattices have been reported. Here we report on the identification of a hexagonal approximant for this QC. Atomically-resolved scanning tunneling microscopy shows the characteristic vertex atoms, which form triangle, square, and rhombus tiling elements, which organize into more complex motifs that are building blocks of the aperiodic QC. Low-energy electron diffraction confirms the large-cell hexagonal structure and is well reproduced by a minimal single-scattering calculation. To accommodate the misfit, the hexagonal layer is twisted $4°$ against the hexagonal Pt(111) substrate, which also lowers the overall symmetry of the system.

I. INTRODUCTION

The discovery of a quasicrystalline phase in a two-dimensional ternary oxide derived from $BaTiO_3$ on Pt(111) opened a new avenue of interest for aperiodic ordering [1–13]. The oxide quasicrystal (OQC) layer itself is only one monolayer in thickness. However, surface science techniques such as scanning tunneling microscopy (STM), noncontact atomic force microscopy (nc-AFM), low-energy electron diffraction (LEED), and surface x-ray diffraction (SXRD), as well as density functional theory (DFT) calculations have not yet been able to unambiguously disclose the atomic structure of this peculiar structure [2–4,10]. As of today, the position of a single atomic species of the OQC seen by local probes on the atomic level has been most thoroughly studied. These atoms form three types of tiles: equilateral triangles, squares, and $30°$ rhombuses. From these basic tiles, dodecagons are formed as characteristic building blocks that are arranged edge-sharing in the quasiperiodic long-range order (with additional triangles and squares, which fill remaining gaps). This dodecagonal tiling, illustrated in Fig. 1, is best described by the mathematical model of Niizeki [14] and Gähler [15]. However, the decoration of these tiles with the two additional atomic species in this ternary compound is currently a matter of debate [2,3,12]. The complete information about the structure is important to understand the growth and stability of the OQC on a fundamental level and to get a hand on its physical and chemical properties. To solve such complex structures, investigations of quasicrystal (QC) approximants are of great importance. Approximants are periodic structures in which the unit cell is given by a patch of the QC thus reducing the structural complexity [16–27].

So far, two approximants have been reported for the OQC that could be fabricated as a single phase: the quadratic σ phase (also known as $3^2.4.3.4$ approximant) [2] and an oblique approximant structure [5]. Their periodically repeating tiling motifs are shown in Fig. 1. Surprisingly until today, no hexagonal approximant has been observed, although the edge-sharing arrangement of dodecagons into triangles as part of the OQC tiling suggests the possibility of a global close-packed arrangement. Such a hexagonal lattice would be closest to the dodecagonal symmetry of the OQC.

The σ-phase approximant is formed by $BaTiO_3$ on Pt(111) and Ru(0001) [2,4,11,12]. In its unit-cell four atoms are seen by STM, which form the vertices of four triangles and two squares as depicted in Fig. 1. This square-triangle tiling is the smallest approximant for the OQC. A combined STM, LEED, SXRD, and DFT study of the σ phase on Pt(111) provided the first model of the atomic structure [2,4]. These first studies concluded that the vertex atoms are formed by Ti, later DFT-based studies proposed a vertex structure of Ba atoms [3], and also a recent complementary experimental study could not resolve this issue [12]. The more complex oblique approximant has been reported in the $SrTiO_3$/Pt(111) system [5]. Its unit cell consists of 24 vertex atoms, which form a tiling of 24 triangles, nine squares, and three $30°$ rhombuses per unit cell. This tiling pattern, which is shown in Fig. 1 and is labeled 24:9:3 approximant in the following, includes a characteristic dodecagonal motif based on two rhombs, five squares, and twelve triangles. Due to its higher complexity it provides a better approximation of the OQC as compared to the σ phase [3,28].

In the following we will show that a long-range ordered hexagonal approximant of the OQC exists. It evolves in two-dimensional layers derived from $BaTiO_3$ on Pt(111) with an unexpected small-angle rotation against the hexagonal substrate [29].

---

[*]mr.maniraj@gmail.com

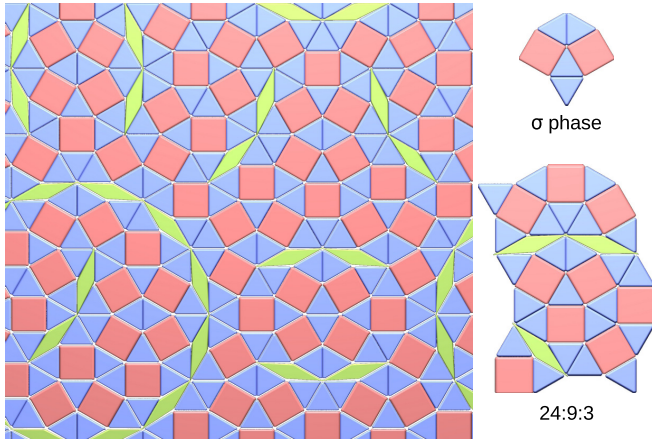[†]stefan.foerster@physik.uni-halle.de

FIG. 1. Dodecagonal triangle-square-rhombus tiling of the OQC (left) and the basic tiling patches of the σ phase and the 24:9:3 approximant. Vertex atoms are located at the corner of the tiling elements.

II. METHODS

Sample growth, LEED, STM and x-ray photoelectron spectroscopy (XPS) measurements were performed at two different ultrahigh vacuum (UHV) chambers at base pressure of better than 1×10^{-10} mbar. Prior to OQC growth, the Pt(111) surface was cleaned by cycles of Ar^+ ion sputtering at 1 keV and a two-step annealing process. In the first step, the crystal was briefly annealed at 1270 K for 30 s to heal out sputter-induced surface roughening. As for the second step, the crystal was annealed at 900 K for 10 min at an oxygen partial pressure of 1×10^{-6} mbar to oxidize residual carbon impurities into volatile CO components. The prepared surface cleanliness was evaluated by monitoring the intensity of C 1s peak in XPS. Temperatures were monitored using a pyrometer (Pyrospot DG40N, DIAS, Dresden) at an emissivity of 0.17. On the clean Pt(111), 1.5 Å of Ba were first deposited at room temperature from a commercial Ba dispenser source (SAES Getters). In the second step, 1.2 Å of Ti were deposited from a Ti rod using a three-cell electron beam evaporator (Focus). Film thickness was estimated using a quartz crystal microbalance maintained at 345 K. Deposited materials were annealed at oxygen partial pressure of 1×10^{-5} mbar for 20 min at 923 K for post-oxidation.

Upon UHV annealing at 1123 K, an OQC monolayer is formed, as characterized by STM and LEED. By heating the OQC monolayer in oxygen (1×10^{-5} mbar, 20 min at 923 K) and UHV ($<5 \times 10^{-9}$ mbar, 5 min at 1123 K) the hexagonal wagon-wheel structure described below is established.

The STM and LEED measurements were conducted at room temperature using a commercial multiprobe SPM (Scienta Omicron, Taunusstein).

Custom code is used for LEED pattern calculation under kinematic scattering conditions with atomic form factor set to unity for all atoms, similar to earlier paper [5]. The unit-cell basis is defined according to the protrusions seen by STM. Calculated single domain pattern is further duplicated, symmetrically rotated and mirrored in according to the substrate symmetry. To compare the calculated pattern with experi-
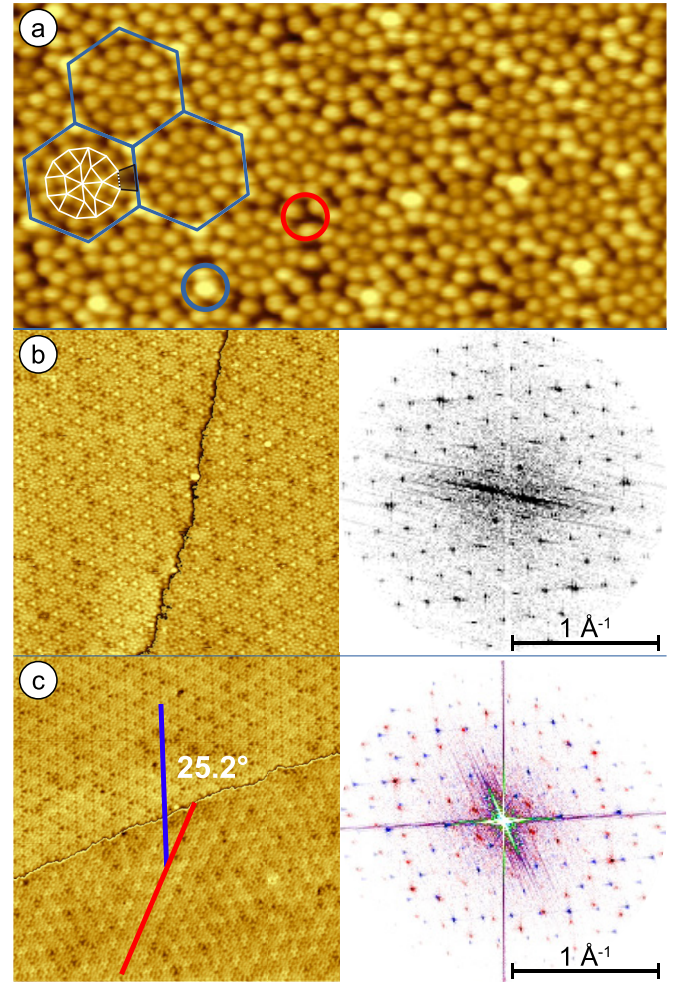

FIG. 2. Atomic resolution STM data of the wagon-wheel structure derived from $BaTiO_3$ on Pt(111). (a) Close-up image with marked Wiegner-Seitz cell (WSC) (blue hexagons) containing a characteristic dodecagon as indicated in white. The corner positions of the WSC can be either occupied or empty (blue and red circles). Representative pictures of two domains meeting at adjacent terraces of the Pt(111) substrate rotated by 0° (b) and 25.2° (c) and the FFT pattern derived from the respective images. Two domains are highlighted by different colors in the FFT pattern in (c). To maximize the contrast in the individual domains, the substrate step has been subtracted from (b) and (c). (a) 24×12 nm², I = 0.5 nA, U = 0.1 V, $\Delta z = 160$ pm. (b) 53×53 nm², I = 0.5 nA, U = 1.0 V, $\Delta z = 240$ pm. (c) 63×63 nm², I = 0.5 nA, U = −1.0 V, $\Delta z = 350$ pm.

ment, the calculated intensities are plotted as 2D Gaussian profiles.

III. RESULTS

Starting from an ideal monolayer of the $BaTiO_3$-derived OQC on Pt(111), an additional cycle of annealing in oxygen (1×10^{-5} mbar, 20 min at 923 K) and UHV ($<5 \times 10^{-9}$ mbar, 5 min at 1123 K) triggers a rearrangement of the material and the formation of a periodic long-range ordered structure.

Figure 2(a) shows an atomically-resolved STM image of a single domain of the wagon-wheel structure. Different

rotational domains homogenously cover the entire crystal. The structure is made up by a hexagonal arrangement of circular motifs interconnected by bridging atoms. The blue hexagons in Fig 2(a) indicate the Wiegner-Seitz cell (WSC) of this structure. Closer inspection identified that the central element of the WSC is a dodecagon filled by twelve equilateral triangles, five squares, and two $30°$ rhombuses [white in Fig. 2(a)]. Taking the bridging atoms between neighboring dodecagons into account, the main motif has a wheel-like appearance, thus it is named as wagon-wheel structure. Please note that neighboring units of these wagon wheels exhibit different rotations identified by the alignment of the two rhombuses. The dodecagon inside the wagon wheel is the characteristic building block of the parent $BaTiO_3$-derived OQC [1,7]. In the OQC, neighboring dodecagons are assembled in an edge-sharing configuration. In contrast, in this wagon-wheel structure, twelve additional atoms are surrounding each of the neighboring dodecagons. These bridging atoms form twelve trapezoids [one is marked black in Fig. 2(a)]. The three short edges of the trapezoids are of the same length as found in triangles, squares, and rhombuses. The long edge is larger by a factor of $(1 + 2 \cdot \sin(15°))$. The dense packing of those tiles results in a triangular cavity at the corners of the WSC as marked by the red circle in Fig. 2(a) and is formed from the long edges of three trapezoids. As marked by the blue circle, these cavities can be occupied with an additional atom. It appears with highest brightness reporting on a significantly larger height above the surface. However, these cavities are also found to remain empty as marked in red in Fig. 2(a).

At the step edges of the Pt(111) substrate the two-dimensional wagon-wheel layer terminates. As a consequence, different domains can be formed on adjacent terraces. Two examples are shown in Figs. 2(b) and 2(c). In Fig. 2(b) the neighboring domains show a parallel alignment, which can be seen also from the Fourier transform (FFT) of the image shown on the right side of the STM image. In contrast, Fig. 2(c) depicts the situation where adjacent domains are differently rotated with respect to the substrate. Between the red and the blue lines, showing the domain orientations, an angle of $25.2°$ has been determined. In the corresponding FFT image, the individual patterns are color coded according to the domain they originate from.

Figure 3 shows the LEED pattern of the wagon-wheel structure taken at energies ranging from 14 eV to 66 eV. At the lowest energy [Fig. 3(a)], a dense set of spots decorates the outline of a hexagon centered at the origin. The corners of this hexagon are defined by two more intense spots at slightly larger reciprocal distance (encircled in blue and magenta). For these spots, a separation of $8°$ has been determined. They originate from two mirror domains of the hexagonal wagon-wheel structure rotated by $\pm 26°$ against the $\langle 1\bar{1}2 \rangle$ direction of Pt(111) [black arrow in Fig. 3(a)]. At larger reciprocal distances, pyramids of 10 spots are observed in the diffraction pattern pointing outwards along the $\langle 1\bar{1}2 \rangle$ directions. Two of them are seen inside the blue rectangle of Fig. 3(b). In between these pyramids, pairs of spots with almost constant spacing guide from smaller to larger reciprocal lengths along $\langle 110 \rangle$ directions. Upon further increase in the kinetic energy of the electrons, a significant number of intense spots appear at
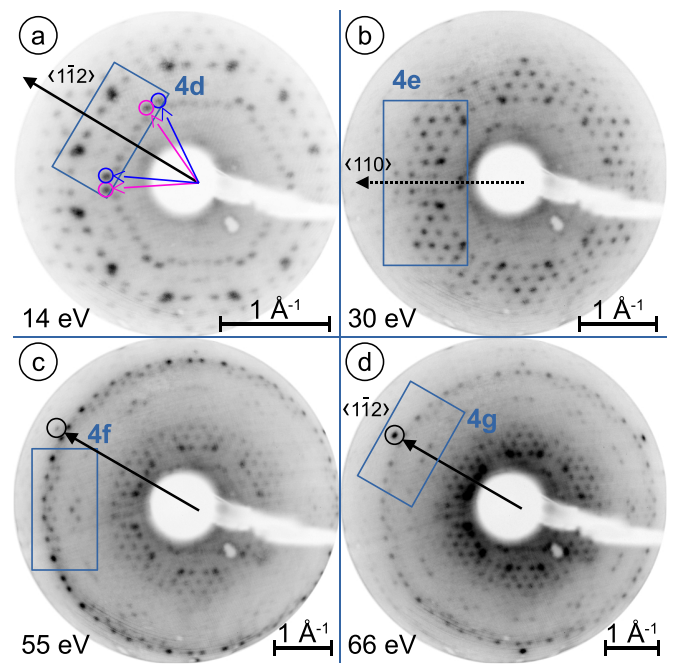

FIG. 3. LEED pattern of the wagon-wheel structure measured at various energies. Magenta and blue arrows mark two mirror domains rotated by $\pm 26°$ against the $\langle 1\bar{1}2 \rangle$ direction of Pt(111) marked by the solid black arrow in [(a),(c),(d)]. Blue boxes in [(a)–(d)] mark regions used for comparison with simulations in Fig. 4

reciprocal distances slightly below $2.62 \, Å^{-1}$, which corresponds to the radius of the first-order diffraction spots of Pt(111) [marked by black circle in Fig. 3(d)].

For a precise determination of the lattice parameters, simulations of the diffraction pattern of the wagon-wheel structure have been performed. As an additional input, the filling of the unit cell has been adopted from the atomically-resolved STM images [Fig. 2(a)]. Due to the close correspondence to the tiling elements of the $BaTiO_3$-derived OQC, namely the presence of the full dodecagon in the unit cell, a similar next-neighbor distance of the protrusions of $6.85 \, Å$ has been initially assumed in the calculations. Accordingly, the lattice vector of the wagon-wheel structure would be $38.8 \, Å$. For a rotation by $26°$ against the Pt(111) lattice this unit cell is $0.3 \, Å$ deviating from a substrate coincidence. Figure 4(a) shows a real-space atomic structure model used for the simulations. Using a next-neighbor distance a_{NN} of $6.80 \, Å$, the wagon-wheel structure forms a commensurate $\left(\begin{smallmatrix} 16 & 7 \\ -7 & 9 \end{smallmatrix}\right)$ super-structure on Pt(111). This results in a hexagonal lattice of the wagon-wheel structure with a periodicity of $38.5 \, Å$, which corresponds to $(2 + \sqrt{3} + 2 \cdot \cos(15°)) \cdot a_{NN}$.

The simulated pattern of a single domain is shown in Fig. 4(b). The calculated intensities are visualized by 2D Gaussian peaks. Black arrows mark the $\langle 1\bar{1}2 \rangle$ direction of the substrate and the black circle sets the scale of the substrate lattice as a guide to the eyes. The wagon-wheel structure produces a dense grid of spots. The first three diffraction orders appear with low intensities. From the fourth-order spots a belt of high-intensity spots is observed. This high intensity of the fourth-order spots is also recognized in the Fourier transform
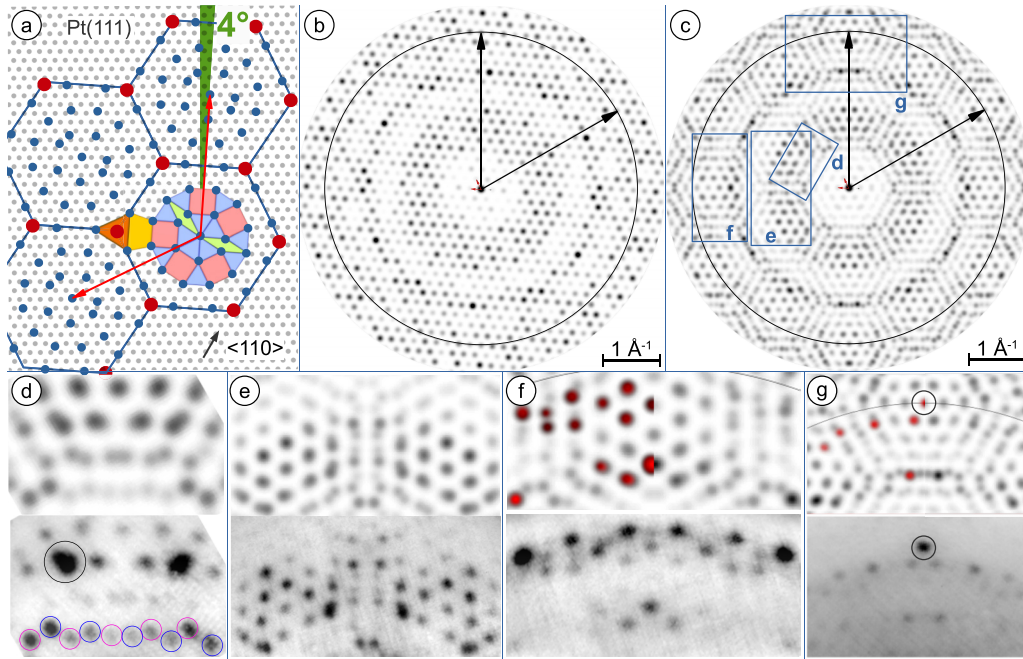
FIG. 4. (a) Model of the wagon-wheel structure on Pt(111). The twist of the 2D layer by 4° against the Pt substrate is highlighted. (b) Simulated diffraction pattern for a single domain and (c) including the mirror domain. The Pt(111) substrate lattice is marked by black arrows. [(d)–(g)] Comparison of characteristic groups of spots in simulations (top) and LEED experiments (bottom). Magenta and blue circles in (d) indicate spots originating from two mirror domains. Red colored region in (f) and (g) marks the experimentally observed spots.

of the STM image shown in Fig. 2(b). Due to the substrate symmetry, a mirror domain must also be taken into account to compare to the measured LEED data. The simulated pattern including this mirror domain is shown in Fig. 4(c). In this superposition of the two hexagonal grids, the regions of high- and low-spot intensities are seen even more clearly. The central features at low reciprocal length are the fourth-order spots that show the splitting of 8° as a consequence of the rotation by 26°, as measured above. The blue frames in Fig. 4(c) mark the regions, which are compared in Figs. 4(d)–4(g) back-to-back with the measured experimental data presented in Fig. 3. The comparison of calculated and experimental diffraction pattern turns out to be excellent despite the fact that only one type of atom of this ternary oxide is considered in the calculation.

The detail in Fig. 4(d) emphasizes the region starting from the fourth-order spots towards higher reciprocal distances. As indicated by the blue and magenta circles all spots of both hexagonal grids can be recognized in the measured pattern. The two elongated intense spots of the experimental data can be assigned to two nearby spots, which are found in the calculations with an identical separation (marked by a black circle). Figure 4(e) focusses on the region of two pyramids of spots seen in experiments. The agreement in the reproduction of the pairs of spots seen in experiment along the central axis is remarkable. It may be noted that one cannot compare the calculated absolute intensity with experimentally observed intensity of equivalent spots due to the fact that the calculations have been carried out under kinematic conditions while in the experimental case dynamic diffraction conditions are unavoidable. Figure 4(f) compares the spots along the intense ring seen in Fig. 3(c) at roughly 2.3 Å⁻¹, slightly

below the Pt(111) substrate spot. The calculated intensities are quite comparable in this region while substantial differences are observed in experiments here. The spots observed in the experiment are colored in red on the left half of Fig. 4(f) and again a perfect match of their positions is found. Finally, Fig. 4(g) compares the region around the substrate spots (marked by black circle). Here the assumed commensurability of the structure can be tested. In the experimental data the intense first-order spot of Pt(111) is observed as the top corner of an equilateral triangle, which is again an exact match to the simulated conditions. For a measurable deviation from this commensurate case, a smearing out of the intensities around the Pt spot would be expected, which is not observed.

Coming back to the alignment of adjacent domains of the wagon-wheel structure two situations are expected. Adjacent domains should either be parallel to each other or in case two mirror domains meet, a rotation of 52° or 8°, respectively, is expected. However, in the STM image of Fig. 2(c) an angle of approximately 25° is reported. This angle indicates that one of the two domains shows a rotation of 26° against the substrate while the other does not. In other words, a nonrotated domain of the wagon-wheel structure can also exist. However, it must be a minority species, since this rotational domain does not contribute to the macroscopic averaging LEED pattern.

IV. DISCUSSION

The hexagonal wagon-wheel approximant is described by a $\begin{pmatrix} 16 & 7 \\ -7 & 9 \end{pmatrix}$ superstructure matrix. From the given dimensions of the unit cell, the density of atoms seen in STM can be determined precisely. In case of an occupation of the large

triangles by adatoms [blue circle in Fig. 2(a)], the unit cell contains 28 vertex atoms, which reduces to 26 if these sites are empty. This results in an area density ranging from $2.02 \, \mathrm{nm}^{-2}$ to $2.18 \, \mathrm{nm}^{-2}$. In comparison, the density of atoms extracted from the $BaTiO_3$-derived OQC is $2.46 \, \mathrm{nm}^{-2}$. This difference is a consequence of an incorporation of tiling element with large area in the unit cell of the wagon-wheel approximant, namely the trapezoid and the large triangle. In contrast, in the OQC tiling these tiles are absent and the frequency of rhombuses, which have the smallest area of all tiles, is higher. The high-temperature treatment that results in the formation of the wagon-wheel structure obviously is accompanied by a change in the chemical composition of this two-dimensional layer. The optional adatom occupation of the two large triangles per unit cell leads to a certain stability window regarding the composition of this particular structure in the two-dimensional ternary oxide.

This wagon-wheel structure differs from other approximants not only by symmetry or the size of the unit cell. Moreover, it is the first approximant including tiles in its unit cell that are not present in the OQC: the trapezoids and the large triangle. The trapezoid exhibits angles of $75°$ and $105°$, whereas all elements within the dodecagonal Niizeki-Gähler tiling have only angles in multiples of $30°$. These angles in increments of $15°$ are responsible for the existence of a second edge length in the tiling, which is the long edge of the trapezoid forming the bigger triangle. This additional edge length is the main reason, why the diffraction pattern of a single domain of the wagon-wheel structure, shown in Fig. 4(b), does not bear any resemblance to the intensity distribution of a dodecagonal diffraction pattern.

On close inspection of the configuration of dodecagons within the wagon-wheel structure, we observe differently rotated dodecagons in the otherwise periodic unit cells. Out of all twelve possible orientations of the central dodecagon, there are only three orientations realized in the wagon-wheel structure as color-coded in Fig. 5(a). Note that in the ideal dodecagonal quasicrystal all twelve orientations are present. However, for the experimentally realized OQC this twelve-fold degeneracy of the dodecagon rotation is lifted and only rotations every $60°$ have been observed [7]. This has been attributed to a stabilization mechanism for the OQC on the three-fold substrate, which is aligned parallel to the edges of the OQC tiling elements. The same holds for the 24:9:3 approximant [5]. In contrast, in the wagon-wheel structure three out of twelve orientations are observed, as seen by coloring the dodecagons in Figs. 5(a) and 5(b). The three different orientations occur with comparable frequency and are related to each other by a $120°$ rotation. However, in the distribution of dodecagons with identical orientation no obvious ordering principle as, e.g., periodic arrangements, can be found. Hence, in terms of the energetics all three local configurations must be degenerate. The most important difference with respect to the OQC and the 24:9:3 approximant is the twist of the wagon-wheel structure by $4°$ with respect to the substrate. Thus we attribute the lifting of the six-fold degeneracy in the rotations of dodecagons to the symmetry breaking of the overall system. This assignment is supported by the observation that in a nonrotated domain of the wagon-wheel structure all
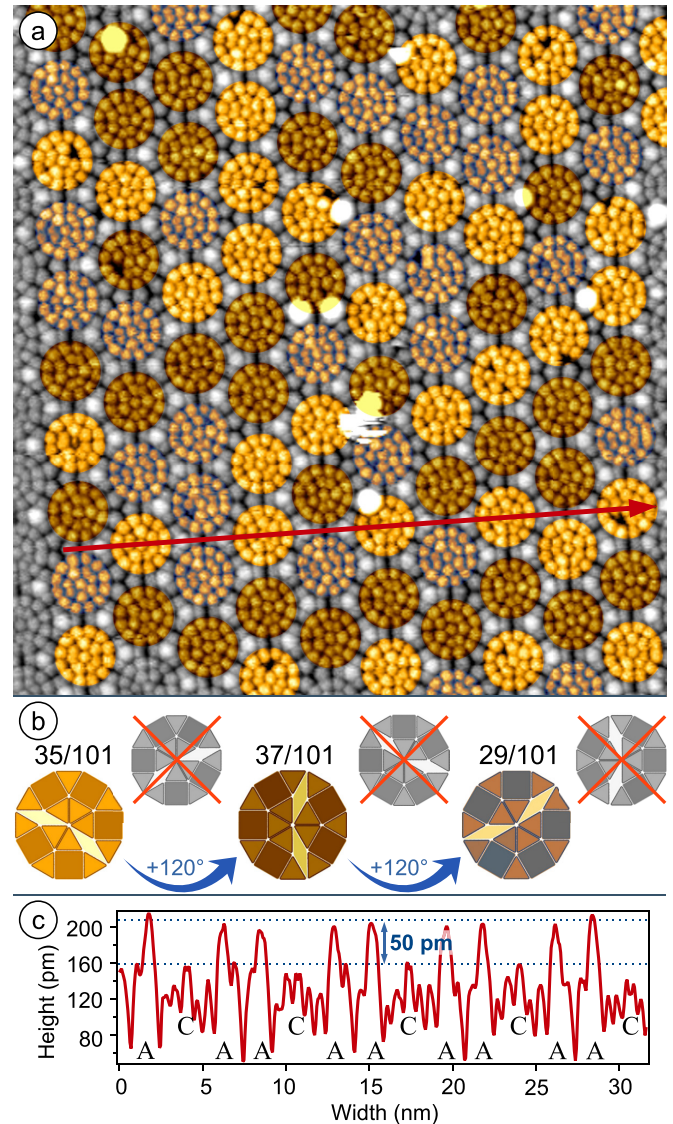

FIG. 5. (a) STM image of the wagon-wheel structure with highlighting of the three distinct rotational orientations of dodecagons. (b) Observed frequencies for each rotation extracted from 101 dodecagons. (c) Line profile extracted along the red arrow in (a). **A** labels adatoms decorating the corners of the WSC, **C** labels the atoms in the center of the WSC. Their heights vary by 50 pm. (a) $37 \times 37 \, \mathrm{nm}^2$, $I = 0.5 \, \mathrm{nA}$, $U = -1.0 \, \mathrm{V}$.

twelve orientations are present as shown in the Supplemental Material [30].

In the STM image of Fig. 5 almost all large triangles are occupied by adatoms. Assuming an identical electronic configuration of the atoms within the plane and the ones decorating the larger triangles, the absolute height difference can be derived from the line profile given in Fig. 5(c). The height difference between these adatoms (marked by **A**) and the central atoms of the dodecagons (marked by **C**) amounts to (50 ± 10) pm. This measurement is calibrated against a monoatomic substrate step covered on both sides with the wagon-wheel structure for which a height of 226 pm has been measured.

V. SUMMARY

The experimental realization of a hexagonal approximant for the dodecagonal Niizeki-Gähler tiling is reported. It is derived from $BaTiO_3$ and forms a commensurate superstructure on Pt(111) with a periodicity of 38.5 Å. The hexagonal overlayer is twisted by $4°$ against the hexagonal substrate. As a consequence, the degeneracy of possible rotations of characteristic dodecagons, which are part of the unit cell, is lifted and only three orientations are found. In contrast to previously reported approximant structures, the unit cell of this hexagonal approximant contains tiles that are not present in the parent OQC. Hence, its diffraction pattern differs significantly from the dodecagonal pattern of the OQC.

[1] S. Förster, K. Meinel, R. Hammer, M. Trautmann, and W. Widdra, Quasicrystalline structure formation in a classical crystalline thin-film system, Nature (London) **502**, 215 (2013).

[2] S. Förster, M. Trautmann, S. Roy, W. A. Adeagbo, E. M. Zollner, R. Hammer, F. O. Schumann, K. Meinel, S. K. Nayak, K. Mohseni, W. Hergert, H. L. Meyerheim, and W. Widdra, Observation and Structure Determination of an Oxide Quasicrystal Approximant, Phys. Rev. Lett. **117**, 095501 (2016).

[3] E. Cockayne, M. Mihalkovič, and C. L. Henley, Structure of periodic crystals and quasicrystals in ultrathin films of Ba-Ti-O, Phys. Rev. B **93**, 020101(R) (2016).

[4] S. Roy, K. Mohseni, S. Förster, M. Trautmann, F. Schumann, E. Zollner, H. Meyerheim, and W. Widdra, The Kepler tiling as the oldest complex surface structure in history: X-ray structure analysis of a two-dimensional oxide quasicrystal approximant, Z. Kristallogr. **231**, 749 (2016).

[5] S. Schenk, S. Förster, K. Meinel, R. Hammer, B. Leibundgut, Maximilian Paleschke, J. Pantzer, C. Dresler, F. O. Schumann, and W. Widdra, Observation of a dodecagonal oxide quasicrystal and its complex approximant in the $SrTiO_3$ -Pt(1 1 1) system, J. Phys.: Condens. Matter **29**, 134002 (2017).

[6] S. Förster, J. I. Flege, E. M. Zollner, F. O. Schumann, R. Hammer, A. Bayat, K.-M. Schindler, J. Falta, and W. Widdra, Growth and decay of a two-dimensional oxide quasicrystal: High-temperature in situ microscopy: Growth and decay of a two-dimensional oxide quasicrystal., Ann. Phys. (NY) **529**, 1600250 (2017).

[7] S. Schenk, E. M. Zollner, O. Krahn, B. Schreck, R. Hammer, S. Förster, and W. Widdra, Full real-space analysis of a dodecagonal quasicrystal, Acta Crystallogr. Sect. A **75**, 307 (2019).

[8] C.-T. Chiang, M. Ellguth, F. O. Schumann, C. Tusche, R. Kraska, S. Förster, and W. Widdra, Electronic band structure of a two-dimensional oxide quasicrystal, Phys. Rev. B **100**, 125149 (2019).

[9] E. M. Zollner, S. Schenk, S. Förster, and W. Widdra, C 60 adsorption on a dodecagonal oxide quasicrystal, Phys. Rev. B **100**, 205414 (2019).

[10] E. M. Zollner, F. Schuster, K. Meinel, P. Stötzner, S. Schenk, B. Allner, S. Förster, and W. Widdra, Two-dimensional wetting layer structures of reduced ternary oxides on Ru(0001) and Pt(111), Phys. Status Solidi B **257**, 1900655 (2020).

[11] E. M. Zollner, S. Schenk, M. Setvin, and S. Förster, Perfect monolayers of the $BaTiO_3$-derived 2D oxide quasicrystals investigated by scanning tunneling microscopy and noncontact atomic force microscopy, Phys. Status Solidi B **257**, 1900620 (2020).

[12] J. Yuhara, K. Horiba, R. Sugiura, X. Li, and T. Yamada, Growth and composition of an ultrathin Ba-Ti-O quasicrystal film and its crystalline approximant on Pt(111), Phys. Rev. Materials **4**, 103402 (2020).

[13] S. Förster, S. Schenk, E. M. Zollner, O. Krahn, C.-T. Chiang, F. O. Schumann, A. Bayat, K.-M. Schindler, M. Trautmann, R. Hammer *et al.*, Quasicrystals and their approximants in 2D ternary oxides, Phys. Status Solidi B **257**, 1900624 (2020).

[14] N. Niizeki and H. Mitani, Two-dimensional dodecagonal quasilattices, J. Phys. A **20**, L405 (1987).

[15] F. Gähler, Crystallography of dodecagonal quasicrystals, *Quasicrystalline materials, in Proceedings of the I.L.L./Codest Workshop, Grenoble, 1988* (World Scientific, Singapore, 1988), pp. 272–284.

[16] V. Elser and C. L. Henley, Crystal and Quasicrystal Structures in Al-Mn-Si Alloys, Phys. Rev. Lett. **55**, 2883 (1985).

[17] C. Henley, Crystals and quasicrystals in the aluminum-transition metal system, J. Non-Cryst. Solids **75**, 91 (1985).

[18] D. C. Koskenmaki, H. S. Chen, and K. V. Rao, Coherent orientation relationship between an icosahedral phase and a cubic α phase in melt-spun Al-Si-Mn, Phys. Rev. B **33**, 5328 (1986).

[19] Christopher, L. Henley, and Veit Elser, Quasicrystal structure of $(Al, Zn)_{49}Mg_{32}$, Philos. Mag. B **53**, L59 (1986).

[20] M. A. Marcus, H. Chen, G. Espinosa, and C.-L. Tsai, Distance distributions about Mn in icosahedral and crystalline Al Mn Si, Solid State Commun. **58**, 227 (1986).

[21] A. I. Goldman and R. F. Kelton, Quasicrystals and crystalline approximants, Rev. Mod. Phys. **65**, 213 (1993).

[22] N. Tamura, The concept of crystalline approximants for decagonal and icosahedral quasicrystals, Philos. Mag. A **76**, 337 (1997).

[23] W. Steurer, The quasicrystal-to-crystal transformation. I. Geometrical principles, Z. Kristallogr. **215**, 323 (2000).

[24] K. Hiraga, T. Ohsuna, W. Sun, and K. Sugiyama, Structural characteristics of Al-Co-Ni decagonal quasicrystals and crystalline approximants, Mater. Trans. **42**, 2354 (2001).

[25] S. Lidin, Quasicrystal Approximants, in *Handbook of Solid State Chemistry* (Wiley-VCH Verlag, Weinheim, Germany, 2017), pp. 73–92.

[26] S. Ranganathan and A. Subramaniam, Orthorhombic rational approximants for decagonal quasicrystals, Bull. Mater. Sci. **26**, 627 (2003).

[27] B. Grushko, D. Holland-Moritz, R. Wittmann, and G. Wilde, Transition between periodic and quasiperiodic structures in Al–Ni–Co, J. Alloys Compd. **280**, 215 (1998).

[28] S. Förster, K. Meinel, K.-M. Schindler, and W. Widdra, Oxygen-deficient ordered phases of ultrathin BaTiO$_3$ films on Pt(111), Surf. Interface Anal. **44**, 628 (2012).

[29] This structure has first been reported in [28] in coexistance with other structures. Please note that the lattice parameters given there are incorrect.

[30] See Supplemental Material at http://link.aps.org/supplemental/10.1103/PhysRevMaterials.5.084006 for a comprehensive analysis of a nonrotated wagon-wheel domain.